

Coherent states for general potentials. V. Time evolution

Vincent P. Gutschick

*Theoretical Division and Life Sciences Division, * Los Alamos Scientific Laboratory, University of California, Los Alamos, New Mexico 87545*

Michael Martin Nieto

Theoretical Division, Los Alamos Scientific Laboratory, University of California, Los Alamos, New Mexico 87545

(Received 26 October 1979)

We show the time evolution of minimum-uncertainty coherent-state (MUCS) wave packets in the solvable potentials we have considered. (Numerical techniques are discussed in the appendices.) The time evolution is compared to the motion that a classical particle would have in the same potential. We make a number of observations on the conditions which can cause the states to lose their coherence more (or less) rapidly with time, and compare the MUCS results with those which can be obtained from other types of coherent states. The most physically interesting comparison is with the "continuous representation" coherent states.

I. INTRODUCTION

In this paper we investigate the time evolution of the minimum-uncertainty coherent-state (MUCS) wave packets which have been derived¹⁻⁶ in the previous four¹⁻⁴ articles of this series. As emphasized in paper III,³ by coherence we mean a state whose wave packet (i) remains localized in position and momentum about the classical quantities, (ii) does not change shape with time, (iii) has an oscillation in position with the classical frequency, and (iv) has an amplitude of oscillation that is the classical amplitude (up to a zero-point contribution).

The coherent states of the harmonic oscillator¹ satisfy all these criteria exactly. Other equally spaced level systems, such as the harmonic oscillator with centripetal barrier (HOCP) potential of paper II and the radial part of the three-dimensional harmonic oscillator, satisfy them approximately, although not exactly. This can be understood by decomposing the coherent states into eigenstates:

$$\Psi_{\text{CS}}(x, t) = \exp(-iHt/\hbar) \sum_n a_n \psi_n(x) \quad (1.1)$$

$$= \sum_n a_n \exp(-iE_n t/\hbar) \psi_n(x). \quad (1.2)$$

For

$$E_n = \mathcal{E}_0(n + \text{const}) \equiv \hbar\omega_c(n + \text{const}), \quad (1.3)$$

one has (j an integer)

$$|\Psi_{\text{CS}}(x, t = t_0 + 2\pi j/\omega_c)|^2 = |\Psi_{\text{CS}}(x, t = t_0)|^2. \quad (1.4)$$

That is, the wave packet regains its original shape after every classical oscillation. (This was discussed in detail for the HOCP potential in paper II.) Thus, any localized wave packet in a sys-

tem satisfying Eq. (1.3) will, after a possible partial dispersion, return to its original shape and position after every classical period. For the HOCP potential of paper II, this could be seen analytically.⁷

However, for systems with nonequally spaced levels, Eq. (1.4) no longer holds and the coherence time is finite.⁸ It is therefore the purpose of this paper to study numerically the time evolution of the MUCS wave packets which we have derived in this series for such systems, and to see what general conclusions can be made from the results.

For the one-dimensional symmetric Pöschl-Teller (PT), symmetric Rosen-Morse (RM), and Morse potentials, our calculations^{2,3} have given us analytic closed forms for the eigenstates, the coherent states, and the decompositions of the coherent states into eigenstates. Thus, in principle the numerical study of the time evolution of the coherent states is straightforward. In practice, however, there are problems. This comes about primarily because the overlap integrals a_n involve differences of extremely large quantities from products of Γ functions of complex arguments with large absolute value. These differences lead to relatively small a_n . (Appendix A describes the numerical procedures which were used.)

In Sec. II we give a number of examples of the time evolution of our MUCS in the above one-dimensional potentials. These examples are presented in the form of computer-generated frames of a movie. Each frame shows (i) the potential, (ii) the wave packet located on a horizontal bar at the energy $\langle H \rangle_{\text{CS}}$, (iii) the number of classical oscillations which have occurred, (iv) a vertical bar located at the particle's classical position, and (v) a spot indicating the mean quantum position $\langle x(t) \rangle_{\text{CS}}$. The figures are all given in terms of the

dimensionless units of energy and position:

$$\mathcal{E}_0 = \hbar^2 a^2 / 2m, \quad z = ax. \quad (1.5)$$

The cases we will discuss are chosen so that the start is midway in time between the classical turning points. We will mention what the differences are if the states start elsewhere.

The examples we give have been selected to demonstrate particular aspects of the results. Some of the phenomena, especially transient phenomena, are more easily demonstrated in actual movies. The present authors and F. Baker⁹ have made such a computer-generated film, which contains more examples than we shall go into here. This film is available, and we shall sometimes refer to it for specific observations.

The time evolution of the radial part of the three-dimensional Coulomb problem, discussed in Sec. III, is more difficult to calculate. This is because the hydrogen atom has a countable infinite number of bound states with an accumulation point at zero total energy. Thus, the number of eigenstates with which a coherent state has significant overlap can sometimes be too large to handle easily. Therefore, in this case we used the more difficult procedure of studying the time evolution of the coherent states by numerically integrating the defining differential equation

$$i \frac{d}{d\tau} \Psi(\rho, \tau) = \mathcal{H} \Psi(\rho, \tau), \quad (1.6)$$

$$\mathcal{H} = - \left(\frac{d^2}{d\rho^2} + \frac{2}{\rho} \frac{d}{d\rho} \right) - \frac{1}{\rho} + \frac{l(l+1)}{\rho^2}, \quad (1.7)$$

$$\tau = 4t\mathcal{E}_0/\hbar, \quad \mathcal{E}_0 = \frac{me^4}{2\hbar^2}, \quad (1.8)$$

$$\rho = r/r_0, \quad r_0 = \frac{\hbar^2}{2me^2}. \quad (1.9)$$

The numerical procedure is discussed in Appendix B.

In Sec. IV we compare our results with some that were obtained from other coherent states. Our final paper¹⁰ will give a set of conclusions that can be made concerning the results of this program.

Before proceeding, we wish to make a few observations on the results obtained, for the reader to bear in mind. As emphasized in paper I¹ and Sec. II of paper II,² it is only for potentials with equally spaced levels that a wave packet can return to its original shape in a period corresponding to one classical oscillation. For not-equally-spaced level systems, such a phenomenon will not occur. In such systems wave packets will dissipate, or lose their coherence, in time.¹¹ This does *not* violate Ehrenfest's theorem, since there¹¹

$$\frac{d}{dt} \langle x \rangle = \frac{1}{m} \langle p \rangle, \quad (1.10)$$

$$\frac{d}{dt} \langle p \rangle = \left\langle -\frac{dV}{dx} \right\rangle = -\frac{d}{d\langle x \rangle} V(\langle x \rangle). \quad (1.11)$$

Also, given a finite coherence time, for any system we will find that the relatively deeper one is in a potential well and, given that, the more eigenstates which have a significant overlap with the coherent state, the longer will be the coherence time.

II. ONE-DIMENSIONAL EXAMPLES

A. Symmetric Pöschl-Teller potential

The symmetric Pöschl-Teller potential of Eq. (II 3.1),

$$V(x) = U_0 \tan^2 z, \quad z = ax, \quad (2.1)$$

$$U_0 = \mathcal{E}_0 \lambda(\lambda - 1), \quad \mathcal{E}_0 = \frac{\hbar^2 a^2}{2m}, \quad (2.2)$$

with eigenvalues

$$E_n = \mathcal{E}_0 (2n\lambda + n^2 + \lambda), \quad (2.3)$$

is contained within an infinite square well with sides at $x = \pm d = \pm \frac{1}{2} \pi/a$. As $\lambda \rightarrow 1$ it becomes an infinite square well. As λ gets large, it looks more and more like a harmonic oscillator near the minimum. (Recall that in the limit $\lambda \rightarrow \infty$, $\lambda a^2 \rightarrow m\omega/\hbar$, it does become a harmonic oscillator.) Our MUCS for this system are given in Eqs. (II 3.15)–(II 3.17) and (II 3.20).

In Fig. 1 we show a coherent-state wave packet in the potential defined by $\lambda = 400$. The value of $C = 89.944i$, where C is defined in Eq. (II 3.17), yields an $\langle H \rangle$ of that of the 10th excited state ($n_{\text{eff}} = 10$). The frames in Fig. 1 are taken $\frac{3}{8}$ of a classical oscillation apart. Thus, in a particular column each frame is $1\frac{1}{2}$ cycles later than the frame above it. The wave packet follows the classical motion of the vertical bar very well. The packet becomes more peaked at the walls, and only begins to show secondary ripples in the frame labeled by $5\frac{1}{4}$ oscillations.

Note that as one goes down the first column the packet becomes wider with time. Also observe that in the frame labeled by $7\frac{7}{8}$ oscillations the dot representing $\langle z(t) \rangle$ is to the right of the vertical classical bar as ripples have developed to the right. But the main peak remains located at the classical vertical-bar position. Finally, with time the MUCS wave packet tends more and more to gather at peaks at the turning points, "sloshing" back and forth between the classical turning points rather than following the classical bar with relatively little change in shape. All the above phe-

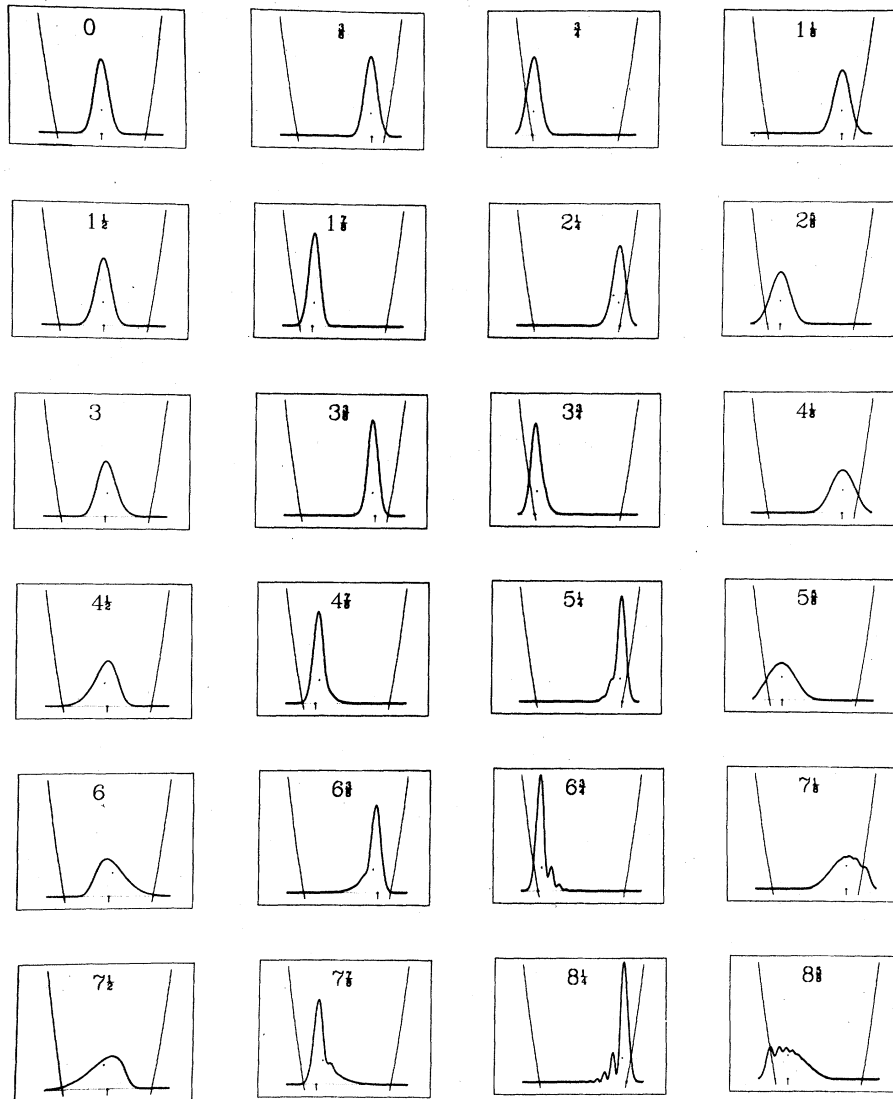


FIG. 1. Time evolution of a coherent-state wave packet in the Pöschl-Teller potential with $\lambda=400$. The state has an $\langle H \rangle$ equal to that of the 10th excited state.

nomena are associated with the gradual loss of coherence and, from our other cases, will be seen to be general features.

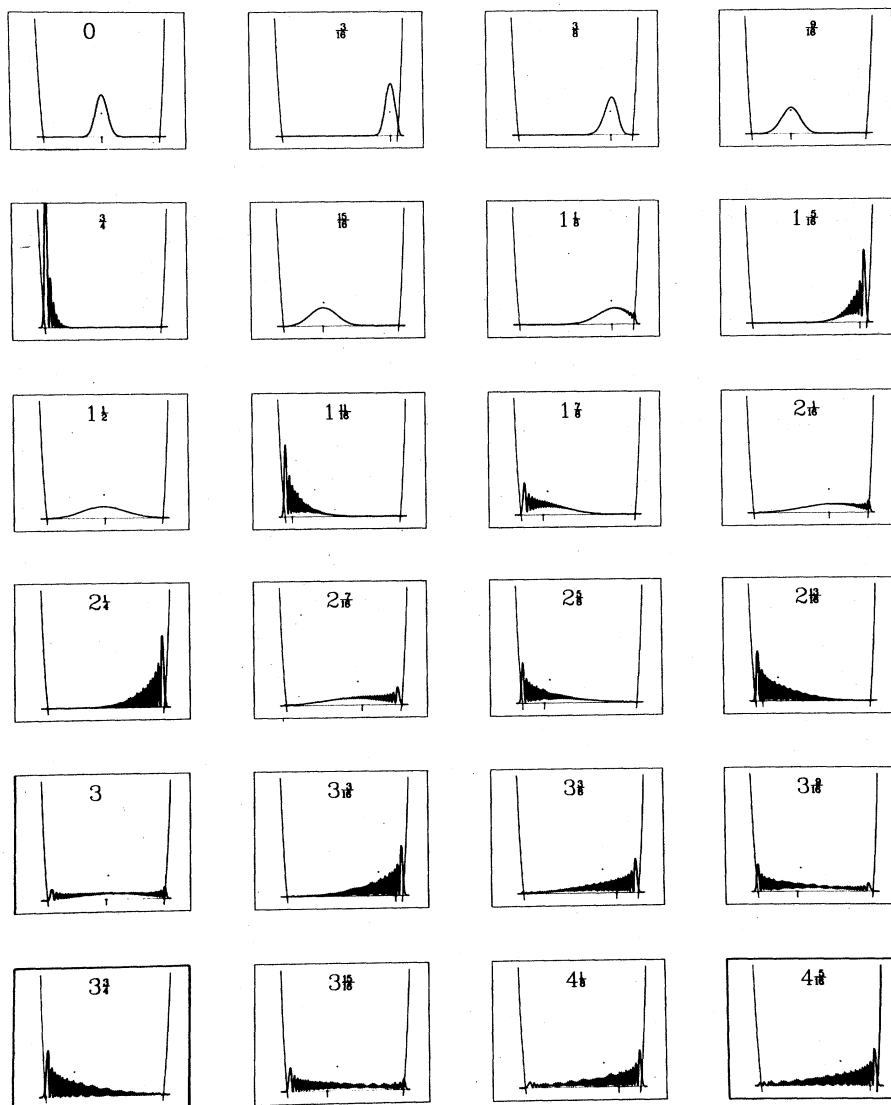
Figure 2 shows a coherent-state wave packet in the potential defined by $\lambda=40$. The value of $C = 80.117i$ gives an $\langle H \rangle$ of that of the 50th excited state ($n_{\text{eff}}=50$). In this confining potential, $\lambda=40$, compared to the $\lambda=400$ of the last example, corresponds to being higher up in the potential and having relatively fewer number states with significant overlap. The sides are steep, and they flatten out quickly to reach zero just below the frames shown. These effects all lower the coherence time (in numbers of classical oscillations) compared to the previous example.

However, one thing which should be emphasized is that we are talking about coherence in terms of number of classical oscillations. The period of these oscillations is potential and energy dependent. From Eqs. (2.2), (2.3), (II3.2), (II3.6), and (II3.19), the classical period τ_c and the classical angular velocity ω_c of Eq. (II3.6) in terms of the n th eigenstate energy are

$$\tau_c = 2\pi/\omega_c, \quad (2.4)$$

$$\omega_c(E_n) = (\lambda+n)(\hbar a^2/m). \quad (2.5)$$

Thus, although a larger λ and a smaller n_{eff} both contribute to longer coherence times in terms of classical oscillations, they have opposite effects



$$E_n = \mathcal{E}_0(2ns - n^2 + s) \quad (2.9)$$

is a potential with a finite number $([s] + 1)$ of bound states, plus a continuum. Our MUCS for this system are given in Eqs. (III 2.17)–(III 2.20) and (III 2.23).

In Fig. 3 we show a coherent-state wave packet in the potential defined by $s = 399.5$, i.e., there are 400 bound states. The state was chosen so that the average energy $\langle H \rangle$ is $\frac{1}{10}$ the way up to the continuum located at U_0 , which gives $n_{\text{eff}} = 20.027$. For a state starting at the potential minimum, $C = 124.98i$. The frames in Fig. 3 are $\frac{3}{8}$ of a classical oscillation apart, so that in a particular column each frame is $1\frac{1}{2}$ cycles later than the frame above

it. The slow loss of coherence is similar to that for the PT case given in Fig. 1, and the same qualitative comments can be made. The main difference is that since this packet has an average energy of the 20th excited state, and Fig. 1 has an average energy of the 10th excited state, the secondary ripples are smaller but more numerous.

Figure 4 shows the same potential with 400 bound states as Fig. 3, but here the average energy $\langle H \rangle$ is $\frac{1}{2}$ the way up to the continuum at U_0 , giving $n_{\text{eff}} = 116.66$. For a starting position at $z = 0$, this is obtained with a value of $C = 282.312i$. From our comments for the PT potential, we expect shorter coherence time in classical oscillations than for the previous example, since we are relatively

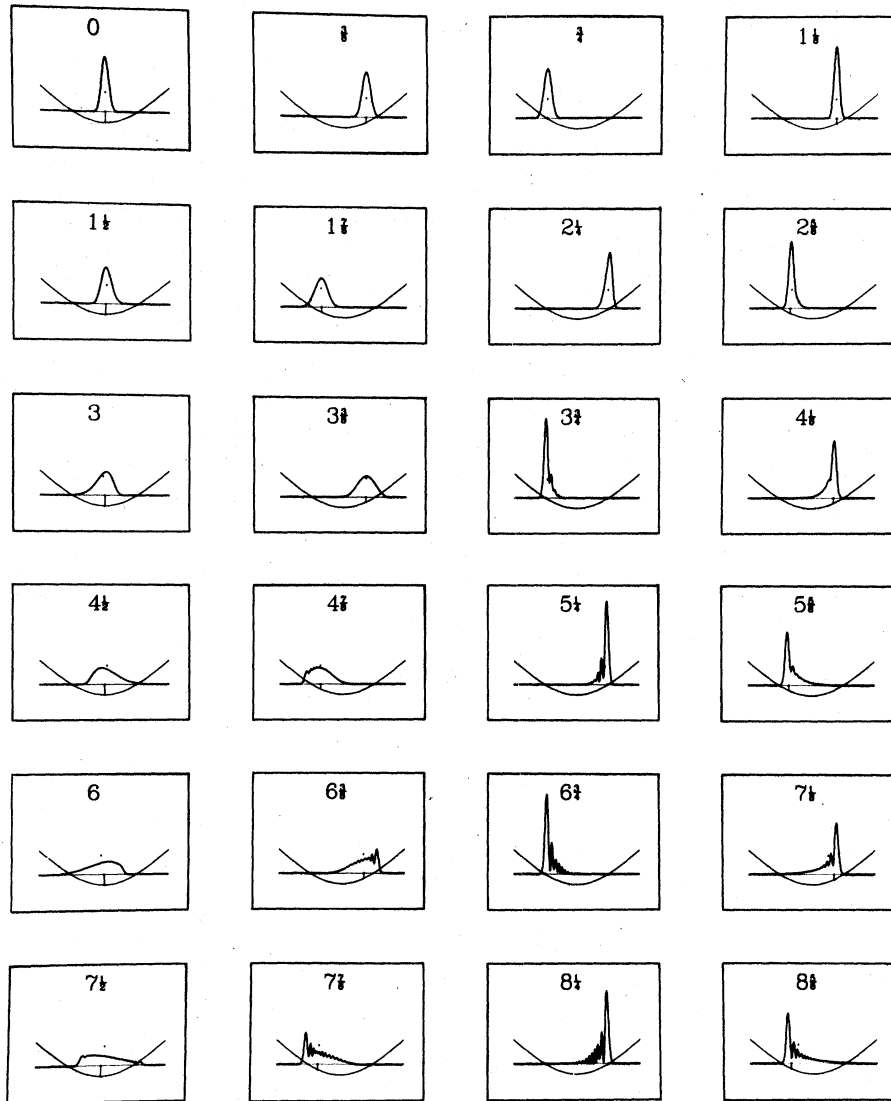


FIG. 3. Time evolution of a coherent-state wave packet in the Rosen-Morse potential with $s = 399.5$ (400 bound states). The state has an $\langle H \rangle$ that is $\frac{1}{10}$ the way up to the continuum at U_0 .

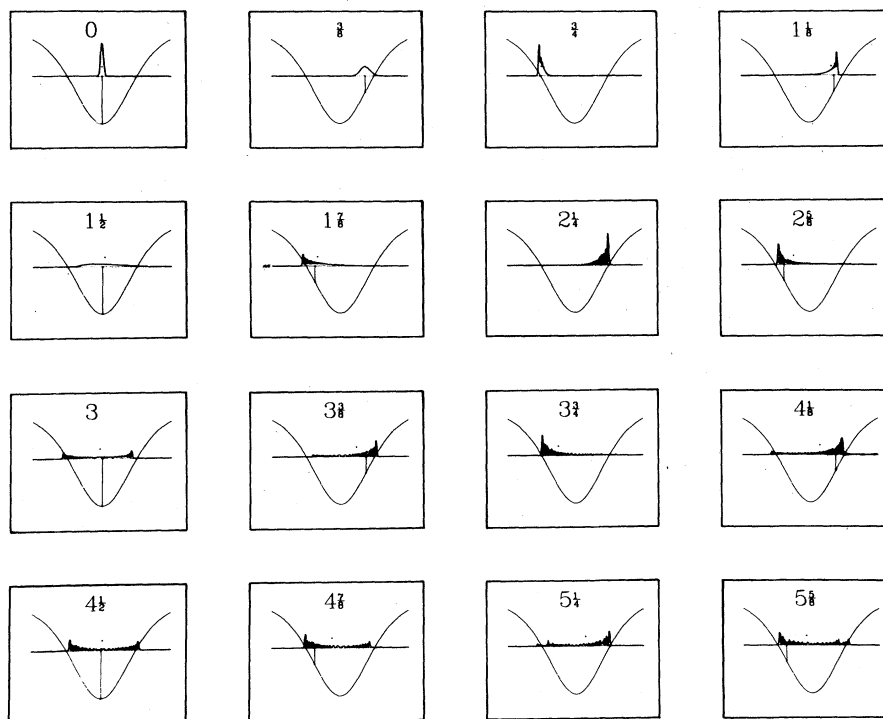


FIG. 4. Time evolution of a coherent-state wave packet in the Rosen-Morse potential with $s=399.5$ (400 bound states). The state has an $\langle H \rangle$ that is $\frac{1}{2}$ the way up to the continuum at U_0 .

higher in the same well. This is seen in Fig. 4.

For comparison with the PT results, the formulas for $\omega_c(E_n)$ and $\omega_\Delta(E_n)$ are

$$\omega_c(E_n) = (s - n)(\hbar a^2/m), \quad (2.10)$$

$$\omega_\Delta(E_n) = n(s - n/2)(\hbar a^2/m). \quad (2.11)$$

Finally, in Fig. 5, we show the time evolution of a coherent-state wave packet in the same potential $s = 399.5$, but with an average energy $\langle H \rangle = \frac{9}{10} U_0$, giving $n_{\text{eff}} = 273$. A start at $z = 0$ is obtained with $C = 379.18i$. This case leads us into a detailed discussion of what occurs as one approaches the

continuum.

For this case, we already have that 7% of the wave packet is in the continuum. It is shown in the first frame by the dotted spike on top of the bound-portion wave packet. The continuum eigenfunctions are $P_s^{\pm i\hbar}(\tanh z)$, which vary as plane waves far away from the potential minimum. Therefore, as discussed in Sec. II of paper III, the continuum contribution to the wave packet evolves off to the sides with time. This state loses its coherence in about one classical oscillation. At times longer than this the movie of this run shows that the quantum expectation-value dot rep-

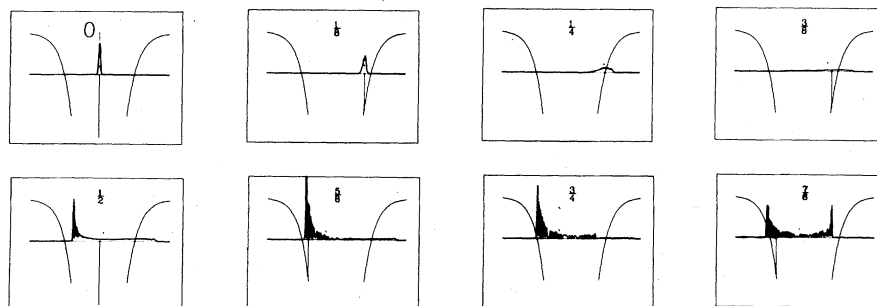


FIG. 5. Time evolution of a coherent-state wave packet in the Rosen-Morse potential with $s=399.5$ (400 bound states). The state has an $\langle H \rangle$ that is $\frac{9}{10}$ the way up to the continuum at U_0 . The wave packet has an expanded vertical scale in the second line.

representing $\langle z(t) \rangle$ develops an amusing jitter about zero.

In addition to having a significant overlap with the continuum, this example also has the bound state with maximum $|a_n|^2$ quite a ways below $n_{\text{eff}} = 273$. It is $n(\text{max}) = 260$, where $n(\text{max})$ labels that eigenstate which has the maximum $|a_n|^2$. To see if this phenomenon was a general one, we did two things.

First we considered wells with on the order of four bound states. Then we could compare our numerical results for $|a_n|^2$ with analytic results based on Eq. (III 2.30). We found that the lowering of $n(\text{max})$ with respect to n_{eff} was a real phenomenon. Even as one goes up so that $\langle H \rangle$ is in the continuum (greater than U_0), $n(\text{max})$ could be lower than the highest bound state.

Next we considered numerically the case $s = 99.5$ with 100 bound states, and took $\langle H \rangle / U_0$ to be closer and closer to the continuum. As shown in Table I, the closer one comes to the continuum, the more overlap there is with the continuum, and the further $n(\text{max})$ decreases below n_{eff} .

Then there was another side to the above phenomenon. Note that all the above cases deal with imaginary C . Positive imaginary C corresponds to coherent states which start at the center of the potential ($z = 0$), moving with maximum velocity to the right at the potential minimum. How do these states compare with other coherent states whose starting points in classical phase space are different? To compare, we looked at coherent states in the same potential with the same values of $\langle H \rangle$, but with C real and positive. This corresponds to classical particles at the right-hand turning points. As seen in Table I, here the contribution to the continuum was less, the number of bound states contributing significantly to the coherent states

was less, and $n(\text{max})$ stayed closer to n_{eff} .

Thus, as one gets near the continuum, the imaginary- C coherent states have more overlap with the continuum (meaning less coherence), but more contributing bound states (meaning more coherence). However, at least for this potential, the net effect is that one obtains a short coherence time as one approaches the continuum no matter if C is real or imaginary.

Also, we observed that even for coherent states deep in the well, where $n_{\text{eff}} \cong n(\text{max})$, for a given $\langle H \rangle$ the larger the real part of C was, the fewer were the number of bound states which contributed significantly to the coherent state.

C. One-dimensional Morse potential

The one-dimensional Morse potential of Eq. (III 3.1),

$$V(x) = U_0(1 - e^{-az})^2, \quad z = ax, \quad (2.12)$$

$$U_0 = \lambda^2 \mathcal{E}_0, \quad \mathcal{E}_0 = \frac{\hbar^2 a^2}{2m}, \quad (2.13)$$

with eigenvalues

$$E_n = \mathcal{E}_0 [2\lambda(n + \frac{1}{2}) - (n + \frac{1}{2})^2], \quad (2.14)$$

also is a potential with a finite number $([\lambda - \frac{1}{2}] + 1)$ of bound states, plus a continuum. However, this potential is asymmetric with the continuum restricted to the right and an exponential barrier on the left. Our MUCS for this system are given in Eqs. (III 3.24)–(III 3.26). For reference, the formulas for $\omega_c(E_n)$ and $\omega_\Delta(E_n)$ are

$$\omega_c(E_n) = (\lambda - \frac{1}{2} - n)(\hbar a^2 / m), \quad (2.15)$$

$$\omega_\Delta(E_n) = n(\lambda - \frac{1}{2} - \frac{1}{2}n)(\hbar a^2 / m). \quad (2.16)$$

In Fig. 6, we show a coherent-state wave packet

TABLE I. Characteristics of coherent states with energies $\langle H \rangle$ near the continuum U_0 , in a Rosen-Morse potential with 100 bound states ($s = 99.5$). Starting positions are at $z = 0$ (imaginary C) and at the right-hand turning point (real positive C). n_{eff} labels the energy in terms of an effective quantum eigenstate number and $n(\text{max})$ labels that eigenstate with the largest overlap with the coherent state. The number of bound states with an overlap probability density at least 10^{-5} is given as well as the overlap with the continuum.

$\langle H \rangle / U_0$	C	n_{eff}	$n(\text{max})$	Number of bound states contributing	Overlap with continuum
0.9	94.578 <i>i</i>	67.9	59	75	0.22
0.9	291.18	67.9	68	30	0.0
0.95	97.198 <i>i</i>	77.1	63	75	0.345
0.95	413.52	77.1	78	28	0.001
0.975	98.482 <i>i</i>	83.7	66	74	0.415
0.975	567.41	83.7	84	26	0.015
0.9875	99.118 <i>i</i>	88.3	66	73	0.450
0.9875	747.92	88.3	88	21	0.063

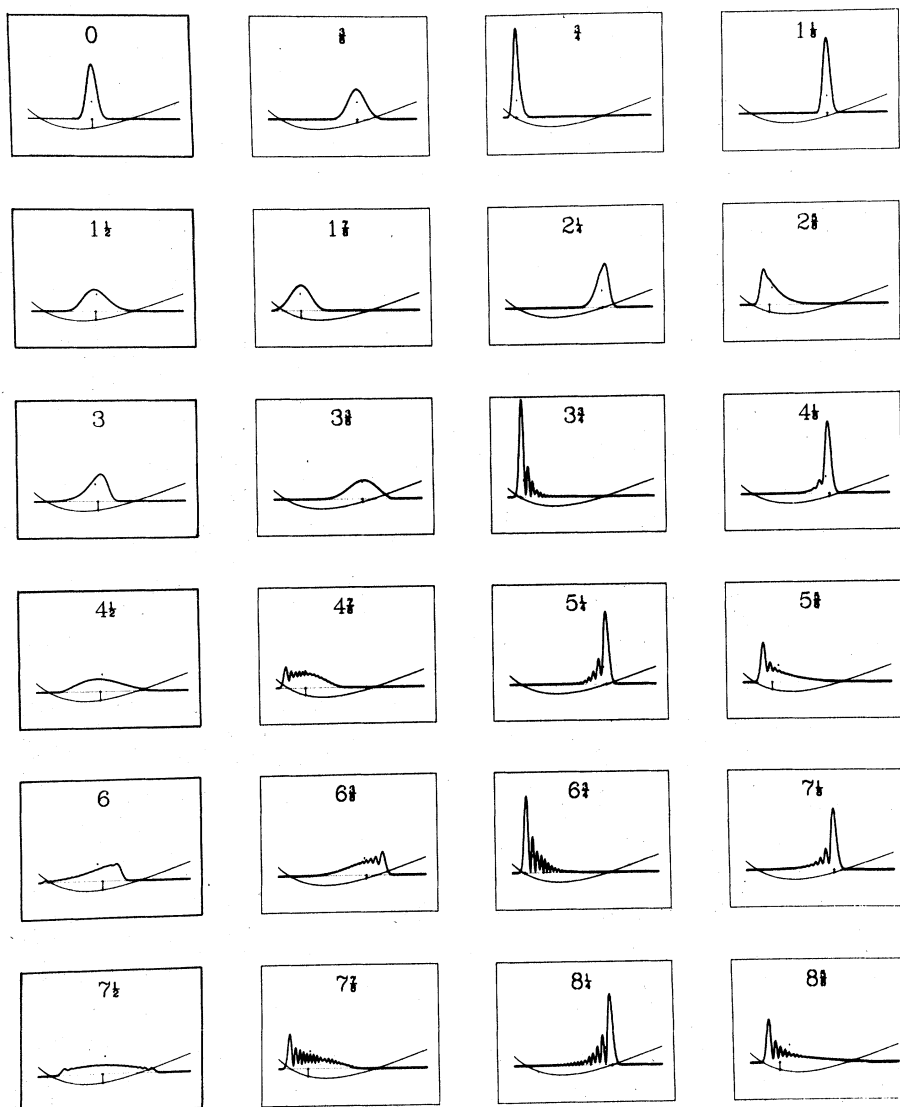


FIG. 6. Time evolution of a coherent-state wave packet in the Morse potential with $\lambda=400$ (400 bound states). The state has an $\langle H \rangle$ that is $\frac{1}{10}$ the way up to the continuum at U_0 .

in the potential defined by $\lambda=400$, i.e., there are 400 bound states. The state was chosen so that the average energy $\langle H \rangle$ is $\frac{1}{10}$ the way up to the continuum located at U_0 , or $n_{\text{eff}}=20.027$. For a state starting halfway in time between classical turning points, the C of Eq. (III.3.20) is $C=(443.274 + 129.933i)$. The frames in Fig. 5 are $\frac{2}{3}$ of a classical oscillation apart, so that in a particular column each frame is $1\frac{1}{2}$ cycles later than the frame above it. This figure is to be compared to Fig. 3 for a coherent state one-half the way up to the continuum in a Rosen-Morse potential with 400 bound states. The reader will observe that frame by frame the two figures are very similar. The slight distortions are due to this potential be-

ing asymmetric about $z=0$, contrary to the symmetric Rosen-Morse potential. Thus, all the comments made for the Rosen-Morse potential coherent state of Fig. 3 also hold here.

Figure 7 now allows us to show the effect of having fewer bound states which overlap with the coherent state. Figure 7 shows a coherent state which also has $\langle H \rangle \frac{1}{10}$ the way up to the continuum at U_0 , but in this case $\lambda=40$ so there are only 40 bound states, meaning $n_{\text{eff}}=1.553$. The net results are that the fringes and size of the wave packet are relatively larger with respect to the distance the classical particle travels, and the coherence time is shorter than in the previous case. (Also, since $\langle H \rangle$ is not much above the ground-

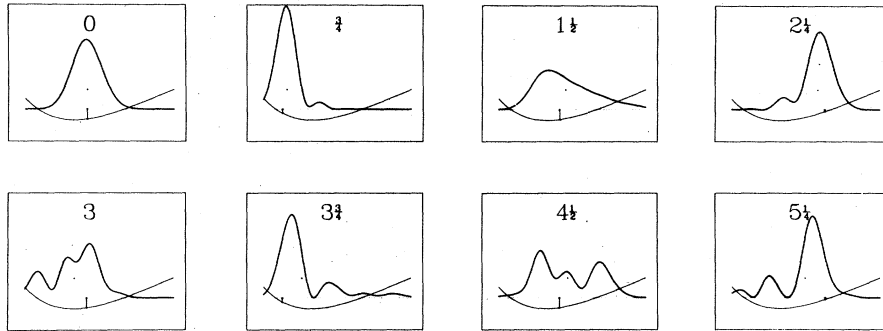


FIG. 7. Time evolution of a coherent-state wave packet in the Morse potential with $\lambda=40$ (40 bound states). The state has an $\langle H \rangle$ that is $\frac{1}{10}$ the way up to the continuum at U_0 .

state energy E_0 , the classical bar visibly does not reach the intercept of the potential with the energy line at $\langle H \rangle$.

Figure 8 again considers the $\lambda=400$ potential with 400 bound states, this time with $\langle H \rangle = \frac{1}{2} U_0$ or $n_{\text{eff}} = 116.66$. $C = (797.01 + 398.50i)$ gives a state halfway in time between the classical turning points. This figure, with each frame $\frac{3}{8}$ of a classical oscillation apart, is to be compared to Fig. 4, showing the similar situation in the symmetric Rosen-Morse potential. Comparing the two figures frame by frame, the reader again can see the similarity, but this time the changes due to the Morse

potential's asymmetry are much larger.

Note that the starting point (midway in time between classical turning points) in Fig. 8 is to the right of the potential minimum. Since the time needed to reach both the right- and left-hand turning points is the same from this position, this means that both the classical particle and the coherent-state wave packet will travel slower going to the right of the starting point than to the left. When one looks at the movie⁹ of this case, this is even more apparent than in this Fig. 8. This phenomenon is a classical manifestation of the effect of the potential's asymmetry. Quantum me-

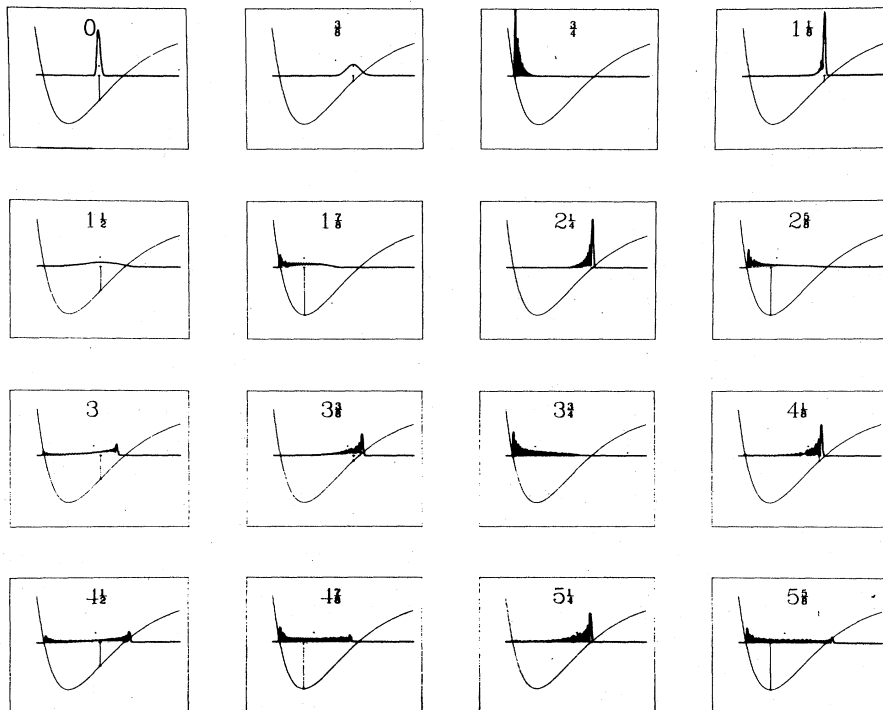


FIG. 8. Time evolution of a coherent-state wave packet in the Morse potential with $\lambda=400$ (400 bound states). The state has $\langle H \rangle$ that is $\frac{1}{2}$ the way up to the continuum at U_0 .

chanically it still shows up in the coherent state's mean position with time, and this asymmetry also changes the wave packet's shape when compared to the Rosen-Morse case of Fig. 4.

III. RADIAL PART OF THE HYDROGEN ATOM

For the radial part of the hydrogen-atom problem, with the centripetal barrier labeled by l , the effective potential and eigenvalues in units of $\mathcal{E}_0 = \frac{1}{4} \mathcal{E}_R$ are

$$V(r) = \mathcal{E}_R \left[\frac{l(l+1)}{\rho^2} - \frac{1}{\rho} \right], \quad \mathcal{E}_0 = \frac{e^2}{4r_0} = \frac{1}{4} \mathcal{E}_R, \quad (3.1)$$

$$\rho = r/r_0, \quad r_0 = \frac{\hbar^2}{2me^2}, \quad (3.2)$$

$$E_n = -\mathcal{E}_0/n^2, \quad n = l+1, l+2, \dots \quad (3.3)$$

In terms of the dimensionless distance ρ , our MUCS are given in Eqs. (IV 4.25) and (IV 4.26).

As discussed in Appendix B, numerical integration of the defining differential equation was used to find the time evolution of the MUCS, and the coherent-state wave packets were then plotted. We found that the time evolution of these Coulomb coherent states was consistent with the time evolution we found for other potentials.

When compared to the one-dimensional Morse potential, the hydrogen atom with centripetal barrier (HACB) potential of Eq. (3.1) has a steeper rise to the left. Therefore, we expect the loss of coherence to be relatively more pronounced, since it was found in the Pöschl-Teller examples that the steeper the barrier the more pronounced was the loss of coherence upon reflection. To the right, the HACB potential rises to the continuum

more slowly (as $1/\rho$) than does the one-dimensional Morse oscillator (as an exponential). Thus, especially for slightly negative $\langle H \rangle$, the states evolve very slowly for large ρ . (Classically, this corresponds to the slow motion of a planet near apogee in an eccentric orbit.) This too leads to loss of coherence, even though many states can have significant overlap.

Given the above modifications, the results we obtained were similar to and consistent with those obtained from the one-dimensional potentials. In Fig. 9 we show one example to demonstrate this.

Figure 9 is for the case where $\langle H \rangle$ is $\frac{1}{5}$ the way up to the continuum at zero energy from the HACB potential minimum of $-\mathcal{E}_0/[l(l+1)]$. For a particle starting halfway in time between the classical turning points, this gives a value for the C of Eq. (IV 4.26) of $(0.002263 - 0.001018i)$. (Note that because of the convention we used in Sec. IV of paper IV,⁴ negative imaginary C means a particle moving to the right.)

The three lines of Fig. 9 should be compared frame by frame to the first three lines of Fig. 8 for a coherent state $\frac{1}{2}$ the way up to the continuum in a one-dimensional Morse oscillator with 400 bound states. The HACB potential is more asymmetric, causing loss of coherence. The significant number of bound states is less in the HACB case. This can be seen by the relatively larger size of the secondary ripples, when they appear, as well as the relatively larger size of the beginning wave packet. Given these distinguishing characteristics, the similarities and differences in the time evolution of the two cases are understandable. Thus, the evolution of the coherent states for the radial part of the hydrogen atom be-

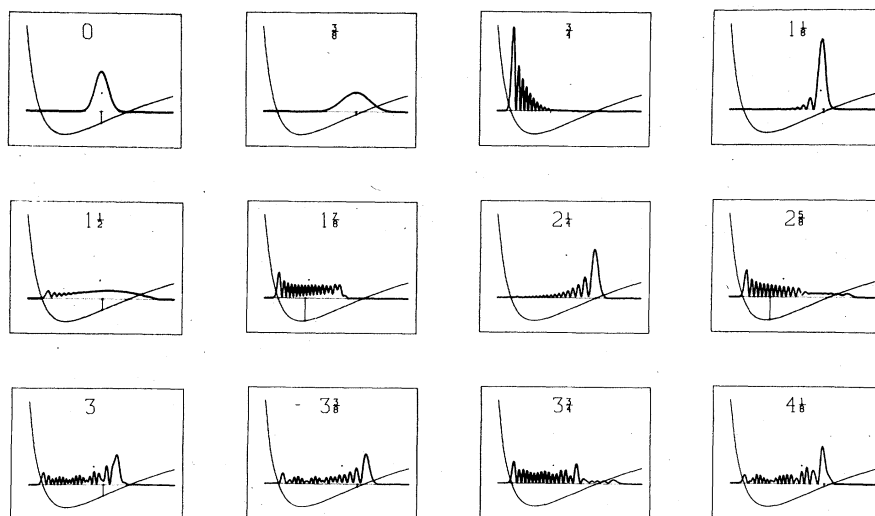


FIG. 9. Time evolution of a coherent-state wave packet in the Coulomb potential with angular momentum barrier defined by $l=150$. The state has an $\langle H \rangle$ that is $\frac{1}{5}$ the way up to the continuum from the minimum.

has as one would have expected from the results of the one-dimensional examples.

IV. OTHER COHERENT STATES

When one thinks of a coherent-state wave packet as a superposition of bound eigenstates, one realizes that one cannot simply draw a bell-shaped curve for the wave packet. Although it gives visual information, a single bell-shaped wave packet at a particular time does *not* describe the system by itself since it is $\Psi^*\Psi$, and hence does not show the complex phase information. This complex phase information tells one what velocity or momentum the packet has.

To see this, simply recall the form of the harmonic-oscillator coherent states given in Eqs. (I 2.8) and (I 2.12):

$$\psi_{\text{CS}}(x) = [2\pi(\Delta x)^2]^{-1/4} \exp\left\{-\left[\frac{x - \langle x \rangle}{2(\Delta x)}\right]^2 + \frac{i}{\hbar} \langle p \rangle x\right\}, \quad (4.1)$$

$$(\Delta x)^2 = \hbar / (2m\omega). \quad (4.2)$$

The condition (4.2) gives the right width to the Gaussian so that the wave packet does not change shape with time and $\langle x \rangle$ determines the starting position. Depending on the values of $\langle x \rangle$ and $\langle p \rangle$, this coherent state can represent a particle of any energy from the ground-state energy $\frac{1}{2}\omega$ up to infinity, and with any initial momentum $\langle p \rangle$. The wave packet, however, does not show the value of $\langle p \rangle$.

These considerations all apply in principle to general potentials. The point is, if one can approximate the shape and phase information of the minimum-uncertainty coherent-state (MUCS) wave functions by some other means, then these different coherent states will evolve in a similar manner. Technically, one either has to have a principle which yields a single-humped wave packet with the proper phase information or else one has to combine bound-state eigenfunctions with coefficients a_n such that all the nodes of the separate eigenfunctions cancel out except for one hump in the wave packet. To start with the eigenfunctions and then cancel out all the nodes is manifestly a much more complicated procedure than to have a principle which yields a single-humped wave packet with proper phase information in the wave function.

The advantage of the MUCS method is that it is a procedure where the wave functions, the decomposition into number eigenfunctions, and the expectation values of interest, such as $\langle H \rangle$ and $\langle X \rangle$, can all be obtained analytically for the exactly solvable examples we have discussed in this

series.

We have also discussed generalizations of other coherent-states techniques which had been used for equally spaced eigenvalue systems. We have called these generalized states annihilation-operator coherent states (AOCS) and displacement-operator coherent states (DOCS). Even though these states are not as analytically tractable as the MUCS, it was of interest to compare them numerically. We did this for the AOCS-DOCS of Eqs. (III 2.59) for the symmetric Rosen-Morse potential. In looking at these states, a problem was that there was no analytic expression for $\langle H \rangle$ or $\langle X \rangle$ as there was for the MUCS. A search procedure had to be used to find an AOCS-DOCS which had a particular starting position in classical phase space and value of $\langle H \rangle$ so that an appropriate AOCS-DOCS could be compared with a particular MUCS.

Given the search procedure, a particular case [$s = 79.5$ (80 bound states), $\langle H \rangle$ being $\frac{1}{4}$ the way up to the continuum at U_0 , and the packet starting at the right-hand turning point] demonstrates the general features of the AOCS-DOCS *vis à vis* the MUCS. At $t = 0$, the MUCS was slightly more localized than the AOCS-DOCS. (The height of the AOCS-DOCS wave packet was 18% less and therefore it was correspondingly broader.) Comparing the two states as they lost coherence and developed secondary ripples with time, the shapes of the two wave packets were very similar (the same number of bumps at roughly the same positions). But the MUCS tended to remain more compact and the AOCS-DOCS lost more probability density to positions far away from the classical position (the main hump of the packet).

Combined with the results of Sec. II, this example alone tells us that after a search procedure has been completed to numerically find AOCS-DOCS with a particular $\langle H \rangle$ and starting position in classical phase space, if the AOCS-DOCS wave-packet shape does not differ too much from the MUCS wave-packet shape, then the AOCS-DOCS time evolution will be similar, if slightly more spread out.

This also implies that the above comments can probably be made about the approximate Coulomb coherent states discussed by Mostowski¹² (which we mentioned in paper IV) if they are compared to our exact, analytic MUCS, whose time evolution we discussed in Sec. III. Also, as we pointed out in paper IV,⁴ our MUCS reduce to the circular-orbit classical states which Brown¹³ obtained on physical bounds. (From our point of view, the circular-orbit case is the ground state of the effective one-dimensional potential.)

Finally, there is another set of states, which we

have not discussed before, which we wish to compare to our MUCS. These are the "continuous representation" coherent states (CRCS) of Klauder.¹⁴ These states are physically interesting to compare with, because in one physical limit they are numerically extremely close to our MUCS, while in another physical limit they are radically different from them.

If x and p are the position and momentum operators, and g and r are constants, the continuous representation coherent states are defined as

$$\psi_{\text{CR}} = \exp[i(xg - rp)]\psi_0(x) \quad (4.3)$$

$$= \exp(-irg/2) \exp(ixg) \exp(-irp)\psi_0(x) \quad (4.4)$$

$$= \exp[i(x - r/2)g]\psi_0(x - r). \quad (4.5)$$

Equation (4.4) is obtained by the use of the Baker-Campbell-Hausdorff identity.

The CRCS wave functions are a displacement *without change of shape* of the ground state, with a particular phase factor added. Since the CRCS are obtained by applying the harmonic-oscillator displacement operator of Eq. (I 2.23) onto the ground state of any system, the CRCS for the harmonic oscillator will be the usual harmonic-oscillator coherent states, as are the MUCS. But how do these CRCS compare to our MUCS for potentials which rise either more slowly or more rapidly than the harmonic oscillator?

For potentials which rise more slowly than the harmonic oscillator, the CRCS can yield almost exact numerical agreement with the MUCS. We demonstrated this by computing many examples in the symmetric Rosen-Morse potential, with starting positions both at $x=0$ and at the right-hand turning points, and for many values of $\langle H \rangle$ including all the very lightly bound cases listed in Table I. Comparing the shapes of the wave packets with time, they almost always overlapped within the width of the oscilloscope's trace of the packets. All the eigenstate overlaps a_n agreed in magnitude and phase to within about 1% of the value of $a_n(\text{max})$. Finally, in cases where the time evolution was followed to many classical oscillations, the CRCS and MUCS wave packets remained on top of each other.

The reason for this agreement can be studied by explicitly writing out the form of the CRCS for this system,

$$\psi_{\text{CR}} = N(0, s) \exp[i(x - r/2)g] \cosh^{-s}[a(x - r)], \quad (4.6)$$

and comparing it with Eq. (III 2.17), the MUCS for this example,

$$\psi_{\text{RM}} = N(C, s) (\cosh z)^{-s} \exp[C \sin^{-1}(\tanh z)] \quad (4.7a)$$

$$= N(C, s) (\cosh z)^{-s} \times \exp\left[\left(u + iv\right)\left(z - \frac{1}{6}z^3 + \frac{1}{24}z^5 + \dots\right)\right]. \quad (4.7b)$$

The CRCS wave packet is centered at $x=r$, always with the shape of the ground state, so its position uncertainty is¹⁵ $(\Delta x)_{\text{CR}}^2 = \Psi'(s)/(2s^2)$, Ψ' here being the trigamma function. The expectation value of momentum is $\langle p \rangle_{\text{CR}} = g\hbar$. On the other hand, the MUCS wave packet has its maximum at $x = [\sinh^{-1}(u/s)]/a$, and has an expectation value of momentum of $\langle p \rangle_{\text{RM}} = va\hbar s |\Gamma(s + \frac{1}{2} + iu)|^2 / |\Gamma(s + 1 + iu)|^2$. Thus, a one-to-one correspondence between (r, g) and (u, v) can be made. (In practice this was done by demanding that $\langle H \rangle$ and $\langle \sinh z \rangle$ were the same for the two sets of states.) Further, any energy MUCS wave packet that has $u=0$ (starting position at the origin) also has the same shape as the ground-state wave packet. What happens when u is not equal to zero is that the asymmetric form of $\exp[2u \sin^{-1}(\tanh z)]$, when multiplying $N^2(C, s)(\cosh z)^{-2s}$, yields a function which numerically is exceedingly close to $\psi_{\text{CR}}^*(x)\psi_{\text{CR}}(x)$.

For potentials rising faster than the harmonic oscillator, however, the CRCS become increasingly nonclassical the faster is the rise. One can realize this by considering the limit of an infinite square-well potential, whose ground state is

$$\psi_0(x) = \left(\frac{2a}{\pi}\right)^{1/2} \cos z, \quad |z| \equiv |ax| \leq \pi/2. \quad (4.8)$$

ψ_0 goes to zero at the sides of the well with one hump. Therefore, the displacement operator $\exp(-irp)$ cannot be applied. Applying $\exp(-irp)$ would give a wave function proportional to $\cos[a(x - r)]$ which does not go to zero at the sides of the well. Further, although giving it a phase factor $\exp(ixg)$ would give the CRCS a higher energy, it still would not be localized and would remain a broad object spread across the entire well. On the other hand, our MUCS can be localized and follow the classical motion in the symmetric Pöschl-Teller potential which limits to the square well when $\lambda \rightarrow 1$.

Therefore, for potentials which have an infinite barrier, such as the infinite square well, the general Pöschl-Teller potential, the one-dimensional Morse potential oscillator on the left, and any radial problem with a centripetal barrier, the CRCS continuous-representation coherent states will begin to fail.

However, it is very instructive and amusing to see on the one hand how well the CRCS approximate the MUCS in potentials which rise as slow as or slower than the harmonic-oscillator potential, whereas on the other hand they begin to fail as one encounters potentials which rise steeply.

ACKNOWLEDGMENTS

We first thank R. P. Feynman for a discussion

concerning what, specifically, we are looking for to have coherence with time. J. Klauder has expressed interest in our problem for some time, and it was at his urging that we compared our minimum-uncertainty coherent states with the continuous-representation states he has investigated. The interesting comparisons mentioned in Sec. IV were the result. Our knowledge of the code used to integrate numerically the differential equation for the Coulomb problem is due, in no small part, to the patient tutoring of Mac Hyman. Finally, of course, our colleague L. M. Simmons, Jr. gave numerous suggestions and comments during the long time over which the work contained in this paper was done. This work was supported by the United States Department of Energy.

APPENDIX A: NUMERICAL METHODS FOR ONE-DIMENSIONAL POTENTIALS

The spatial wave function $\Psi_{\text{CS}}(z, t)$ for a given coherent state is calculable from the eigenstate wave functions $\psi_n(z) \equiv N_n \phi_n(z)$, the eigenenergies E_n , and the set of initial amplitudes $\{a_n\}$. Analytic expressions exist for all three of these quantities for the potentials we have considered. However, actual calculations of numerical values of wave functions demand more effort than is apparent.

The eigenfunctions $\psi_n(z)$ are most economically generated from ψ_0 by using the recursion relations for the special functions involved. Each $\psi_n(z)$ must be calculated numerically over the range $[z_L, z_R]$ where the coherent state has significant magnitude. $[z_L$ and z_R were chosen by simple criteria which guaranteed covering the range wherein Ψ had "significant" magnitude (roughly $\geq 10^{-2}$ of peak).]

When more than approximately 100 eigenstates are required to represent $\Psi(z, t)$, the recursion becomes difficult numerically. Specifically, $\psi_0(z)$ at $z \approx z_L$ or $z \approx z_R$ commonly attains a magnitude below that which is representable on a digital computer, even a computer such as the CDC 6600 which can represent 10^{-322} . At such coordinate values ψ_0 would be represented as zero and recursion from ψ_0 would erroneously yield zero values for all ψ_n at the same z value. Thus, we resorted to renormalizing the recursions by $[\psi_0(z)]^{-1/2}$, and then at the end multiplying all "provisional" $\psi_n(z)$ by the factor $[\psi_0(z)]^{1/2}$.

For calculating numerical values of the a_n , straightforward use of the analytical formulas is satisfactory up through moderate values of n , typically 30–50. At larger values of n , the cancellation of terms of alternating signs reaches such extremes as to prohibit retention of one significant digit in a_n . (The correctness of the analytical formulas was, of course, verified for cases where fewer than 30–50 eigenstates contributed

significantly. The spatial wave functions were compact, bell-shaped, and they moved with the correct classical period of oscillation.) For these large cases, we resorted to numerical integration:

$$a_n = \int_a^b dz \psi_n(z) \Psi_{\text{CS}}(z, 0). \quad (\text{A1})$$

For use in Eq. (A1), one needs a numerically stable computation of $\Psi_{\text{CS}}(z, 0)$. In the analytic formulas (II 3.15), (III 2.17), and (III 3.24) the separate factors such as Γ functions or high powers of the special functions of z tend to be unrepresentably large or small on a computer at large z or when large values of the potential parameters λ or s are involved. Separate computations of the logarithms of each factor sufficed, making the final step the exponentiation of the algebraic sum of logarithms.

Because for large n the ψ_n span a large range of z and because they oscillate $n - 1$ times, accurate evaluation of a_n requires that the integration limits a and b be as close as practical to the asymptotes of the physical problem and that the spacing of points z be fine enough to get several points per node in ψ_n (we used eight). However, the central range of $[z_L, z_R]$ deserves the densest sampling of points. It is here that the principally contributing ψ_n have their maximum amplitudes. Therefore, we employed coordinate transformations in the above integral in order to satisfy all three criteria and still use a tractable number of points (3000 or less).

For example, in the Rosen-Morse problem, the asymptotes are $(-\infty, \infty)$ whereas $-z_L$ and z_R are typically of order unity. We employed the coordinate transformation

$$z = \cosh^{-1}(\cos y), \quad (\text{A2})$$

$$y = \sin^{-1}(\tanh z), \quad (\text{A3})$$

$$a_n = \int_{-\infty}^{\infty} dz \psi_n(z) \Psi_{\text{CS}}(z, 0) \quad (\text{A4})$$

$$= \int_{-\pi/2}^{\pi/2} \frac{dy}{\cos y} \psi_n(y) \Psi_{\text{CS}}(y, 0). \quad (\text{A5})$$

Both ψ_n and Ψ_{CS} have simple mathematical forms in both z and y spaces. The points in y were spaced evenly for a Simpson-rule integration.

Given the a_n , the coherent-state wave function $\Psi_{\text{CS}}(z, t)$ can be computed for arbitrary time. However, for cases of interest involving large numbers of contributing states, straightforward numerical summation of $a_n \psi_n(z) \exp(-iE_n t/\hbar)$ over all n would involve storage of values of $\psi_n(z)$ for a grid of rank 400 in n by 400–600 in z . This exceeds virtually any practical computer core storage. To circumvent this, we stored values of $\psi_n(z)$ on disk as separate vectors over all n at

fixed z . Reading in, storing, and computing with only one such vector then sufficed to calculate $\Psi_{\text{CS}}(z, t)$ at a single point z . In actual computer-generated plots of $\Psi_{\text{CS}}(z, t)$, we generated smooth curves from the basic grid by using available spline-based interpolation algorithms.

The spacing of points in z at which Ψ_{CS} was computed was chosen to be approximately $\frac{1}{4}$ the intermodal distance in $\psi_N(z)$, where

$$E_n \equiv g(n), \quad (\text{A6})$$

$$N = n_{\text{opt}} \cong g^{-1}(\langle H \rangle). \quad (\text{A7})$$

The next task was choosing the complex parameter $C = u + iv$ to yield the desired value of $(\langle H \rangle - E_0)$ (trivial) and the desired phase θ , corresponding to E_c and θ_c , respectively, for the classical particle. (The convention we use is that $\theta = 0$ corresponds to the midpoint in time between turning points, with the packet moving to the right.) Because of the ground-state contribution to the quantum $\langle H \rangle$, in general, there is no unique and exact analytic method for inverting the classical equations

$$X_c = A(E) \sin[\omega_c(E)t], \quad (\text{A8})$$

$$P_c = m\omega_c(E)A(E) \cos[\omega_c(E)t], \quad (\text{A9})$$

to obtain the quantum analog with a unique $C = u + iv$ and $\langle H \rangle$. This significantly affects only coherent states with $\langle H \rangle$ close to E_0 . As a result, the following approximate method could be used, which is best discussed in terms of a concrete example, the Pöschl-Teller potential.

The turning-point values u_L and u_R are chosen such that $\langle H \rangle$ has the desired value with $v = 0$. We then took it that u corresponding to any phase θ obeys

$$u = \left(\frac{u_L + u_R}{2} \right) + \left(\frac{u_R - u_L}{2} \right) \sin\theta \\ = u_{\text{mid}} + \delta u \sin\theta. \quad (\text{A10})$$

(For the symmetrical Pöschl-Teller case, $u_L = -u_R$, but the form above hints at the general case.) The value of v is set by $\langle H \rangle$.

The final numerical task was calculating the position z_c of the corresponding classical particle. For the PT case, to be consistent with our choice of C , we effectively computed a $u(t)$, given by

$$u(t) = u_{\text{mid}} + \delta u \sin(\omega_c t + \theta_c), \quad (\text{A11})$$

and used this to calculate $\sin z_c$, and hence z_c . Similar schemes were used on the other potentials.

APPENDIX B: NUMERICAL METHODS FOR THE COULOMB POTENTIAL

In principle, numerical calculation of the time-evolved Coulomb coherent-states wave functions could be performed by the methods used for one-dimensional potentials; that is, $\Psi(\rho, t)$ could be resolved into eigenstate components. However, since the Coulomb potential has a countably infinite number of bound states with an accumulation point at the continuum, as one goes up in energy the number of eigenstates with which a coherent state has significant overlap can become too large for an efficient numerical calculation. Therefore, direct numerical integration of the reduced Schrödinger equation was done by finite differences.

Writing the Schrödinger equation in terms of time-derivative and spatial operators as

$$\frac{d\Psi}{dt} = \hat{\mathcal{O}}_t \Psi = \hat{\mathcal{O}}_\rho \Psi, \quad (\text{B1})$$

one finds that the finite-difference operator approximating $\hat{\mathcal{O}}_\rho$ has imaginary local eigenvalues. A choice of finite-difference operator for $\hat{\mathcal{O}}_t$ is required which is stable for imaginary eigenvalues and which achieves high numerical accuracy with minimal computing effort. Such a choice is the "leap-frog corrector method" with a single correction step.¹⁶ Defining Ψ^0 and Ψ^1 as initial and corrected approximate wave functions, and denoting the n th discrete time value as t_n , we have

$$\Psi^0(\rho, t_{n+1}) = \Psi^1(\rho, t_{n+1}) + 2\delta t \hat{\mathcal{O}}_\rho \Psi^1(\rho, t_n), \quad (\text{B2})$$

$$\Psi^1(\rho, t_{n+1}) = \frac{4}{5} \Psi^1(\rho, t_n) + \frac{1}{5} \Psi^1(\rho, t_{n-1}) \\ + \frac{1}{5} \delta t [2\hat{\mathcal{O}}_\rho \Psi^0(\rho, t_{n+1}) + 4\hat{\mathcal{O}}_\rho \Psi^1(\rho, t_n)]. \quad (\text{B3})$$

The (uniform) spatial step size $\delta\rho$ was chosen rather intuitively to be roughly $\frac{1}{4}$ the period of the finest spatial variation in long-time evolution; i.e., $\frac{1}{2}$ the internodal distance of the highest eigenstate which contributes significantly to the coherent state. For example, with l of the order of 100 and $\langle H \rangle = \frac{1}{2} V(\rho_{\text{min}}) = (\frac{1}{2} \text{ up to the continuum from the potential minimum})$, this meant using up to 500 or 600 points in ρ . In order to ensure stability of the temporal integration, the time step δt must satisfy the Courant condition,

$$\delta t < \text{const} \times \text{local eigenvalue of } \hat{\mathcal{O}}_\rho. \quad (\text{B4})$$

$$\leq \min \left[\frac{1}{2} \delta\rho^2, \frac{3}{2} \rho_{\text{min}} \delta\rho, \frac{3}{2} \rho_{\text{min}}, \frac{3}{2} \frac{\rho_{\text{min}}^2}{l(l+1)} \right]. \quad (\text{B5})$$

We further enforced a safety factor of $\frac{1}{2}$ in the latter approximate form. To evolve five classical oscillations the number of time steps needed was typically 1000–20 000. During the temporal integration, we occasionally tested the normalization of

Ψ as calculated by Simpson-rule spatial integration. The integration was terminated and rerun at smaller ($\delta\rho, \delta t$) if any significant deviation from unity occurred.

The finite spatial region $[\rho_L, \rho_R]$ over which we calculated Ψ was chosen such that $\rho^2 |\Psi|^2$ at any point in time evolution never attained a significant magnitude at the end points. A usable criterion proved to be choosing ρ_L such that for the leftmost-starting coherent state of the given energy E , i.e., $\Psi(\rho_L, t=0; \langle H \rangle = E, C = u_L)$, the magnitude of $\rho^2 |\Psi|^2$ at ρ_L was 10^{-6} its value at the peak. ρ_R was chosen similarly, with a rightmost-starting packet. Simple Newton-Raphson root-finding techniques sufficed. (Loosening of the 10^{-6} criterion led to induced oscillatory errors in Ψ when the packet evolved toward the boundaries.)

A five-point difference approximation to $\hat{\rho}$ was chosen as an optimal compromise between accuracy and computing effort. At points immediately bordering the boundaries where Ψ was set equal to zero, a three-point difference formula was used.

Numerically stable computation of the initial $\Psi(\rho, 0)$ from the analytic formula (IV 4.25) requires some care. Separate factors such as high powers of ρ or Γ functions tend to be unrepresentably large or small on a computer for extreme values

of ρ or large values of l . Separate computations of the logarithm of each factor sufficed, making the final step the exponentiation of the algebraic sum of logarithms.

The complex parameter C was chosen for the best correspondence of coherent motion with classical motion at the same energy $\langle H \rangle = E_c$ and at a chosen phase $\theta = \theta_c$. (Contrary to our practice in the one-dimensional potentials, we did not subtract the zero-point energy, which was quite negligible in cases of interest.) The classical analytical equation for the initial value of ρ as a function of E_c and θ_c [paper IV, Eq. (B16)] was solved by Newton-Raphson root-finding techniques, with some complicated constraints to stabilize the search. Given this value of ρ , we then chose the value of u to give the identical value for the quantum expectation $\langle \rho \rangle$. The magnitude of v was set to satisfy $\langle H \rangle = E_c$, and its sign was determined by the convention that at a phase of zero the packet is rightward-moving and at the midpoint in time between turning points.

For all times greater than zero, the classical $\rho(t, E, \theta_0)$ and the quantum $\langle \rho \rangle$ were computed and compared. The classical ρ was computed by again iteratively solving the classical analytical equation. The quantum $\langle \rho \rangle$ was computed by Simpson-rule integration.

*Present address.

¹M. M. Nieto and L. M. Simmons, Jr., Phys. Rev. D **20**, 1321 (1979) (paper I, on the formalism).

²M. M. Nieto and L. M. Simmons, Jr., Phys. Rev. D **20**, 1332 (1979) (paper II, on confining one-dimensional examples).

³M. M. Nieto and L. M. Simmons, Jr., Phys. Rev. D **20**, 1342 (1979) (paper III, on nonconfining one-dimensional examples).

⁴M. M. Nieto, preceding paper, Phys. Rev. D **22**, 391 (1980) (paper IV, on three-dimensional systems).

⁵Separate individual papers on this topic are M. M. Nieto and L. M. Simmons, Jr., Phys. Rev. Lett. **41**, 207 (1978); Phys. Rev. A **19**, 438 (1979); and in *Foundations of Radiation Theory and Quantum Electrodynamics*, edited by A. O. Barut (Plenum, New York, 1980), pp. 199-214.

⁶Work on related aspects of quantum mechanics is in M. M. Nieto, Phys. Rev. A **17**, 1273 (1978); M. M. Nieto and L. M. Simmons, Jr., Am. J. Phys. **47**, 634 (1979); M. M. Nieto, Phys. Rev. A **20**, 700 (1979); Am. J. Phys. **47**, 1067 (1979).

⁷Y. Weissman and J. Jortner [Phys. Lett. **70A**, 177 (1979)] considered a Gaussian state in the HOCB potential. Leaving aside the fact that the Gaussian yields $\langle H \rangle = \infty$ because of the potential spike at the origin, all Gaussians are not coherent states even for the real harmonic oscillator. The subset of Gaussians with

the width of the ground state $(\Delta x)^2 = \frac{1}{2}\hbar/m\omega$ are the coherent states of a particular harmonic oscillator. (See paper I.¹) We have commented on this and our MUCS for the HOCB potential in V. P. Gutschick, M. M. Nieto, and L. M. Simmons, Jr., Phys. Lett. **76A**, 15 (1980).

⁸From the theory of almost periodic functions, if one waits long enough any state which has a significant overlap with a finite number of eigenstates will eventually return to "almost" its original shape. This is the time when tE_n/\hbar is almost an integral number times 2π for all the eigenstates "n" with which the state has a significant overlap. In general, this time is very large, and we shall not concern ourselves with this phenomenon. It amounts to having a totally dispersed wave packet suddenly regenerate itself after very long times.

⁹V. P. Gutschick, M. M. Nieto, and F. Baker, *Time-Evolution of Coherent States for General Potentials*, 13 min., 16 mm, color, sound movie, available from Cinesound Co., 915 N. Highland Ave., Hollywood, California 90038. Copies are on deposit at the AAPT and Los Alamos Scientific Laboratory film libraries. A review of the film is given in C. A. Nelson, Am. J. Phys. **47**, 755 (1979).

¹⁰M. M. Nieto, L. M. Simmons, Jr., and V. P. Gutschick (in preparation). This will be the final article of this series, giving our conclusions.

- ¹¹See, for example, the discussions in Yu. E. Murakher, Dokl. Akad. Nauk SSSR 165, 526 (1965) [Sov. Phys. Dokl. 10, 1079 (1966)], and K. Eswaran and P. M. Mathews, J. Phys. A 7, 1547 (1974). A discussion of Ehrenfest's theorem is in A. Messiah, *Quantum Mechanics* (North-Holland, Amsterdam, 1959), Vol. I, p. 216.
- ¹²J. Mostowski, Lett. Math. Phys. 2, 1 (1977).
- ¹³L. S. Brown, Am. J. Phys. 41, 525 (1973).
- ¹⁴J. R. Klauder, J. Math. Phys. 5, 177 (1964); in *Path Integrals and their Applications in Quantum, Statistical, and Solid State Physics*, edited by G. J. Papadopoulos and J. T. Devreese (Plenum, New York, 1978), pp. 5-38.
- ¹⁵See Eq. (2.18) in M. M. Nieto, Phys. Rev. A 20, 700 (1979). In Eq. (2.17b), $\Gamma(s=\frac{1}{2})$ should be $\Gamma(s+\frac{1}{2})$.
- ¹⁶J. M. Hyman, in *Advances in Computer Methods for Partial Differential Equations-III*, edited by R. Vichnevetsky and R. S. Stepleman (IMACS, Bethlehem, Penn., 1979), pp. 313-321. See Eq. (6.8) on p. 319.